Comprehensive Analysis of Glulam Delamination Though Finite Element Modelling Incorporating Physical and Mechanical Properties: A Case Study Using High Density Hardwood

Peiqing Lu (peiqing.lu@griffithuni.edu.au)
Griffith University
Benoit P. Gilbert
Griffith University
Chandan Kumar
Queensland Government Department of Agriculture and Fisheries, Forest Products Innovation, Salisbury Research Facility
Robert L. McGavin
Queensland Government Department of Agriculture and Fisheries, Forest Products Innovation, Salisbury Research Facility
Hassan Karampour
Griffith University

Research Article

Keywords: glued laminated timber, moisture content, fracture, delamination, drying stress

Posted Date: January 24th, 2024

DOI: https://doi.org/10.21203/rs.3.rs-3886752/v1

Additional Declarations: No competing interests reported.

COMPREHENSIVE ANALYSIS OF GLULAM DELAMINATION THOUGH FINITE ELEMENT MODELLING INCORPORATING PHYSICAL AND MECHANICAL PROPERTIES: A CASE STUDY USING HIGH DENSITY HARDWOOD

Peiqing Lu[1, *], Benoit P. Gilbert[1,2], Chandan Kumar[2], Robert L. McGavin[1,2], Hassan Karampour[1]

[*]Corresponding author

[1] School of Engineering and Built Environment, Griffith University, Gold Coast, QLD 4222, Australia

[2] Queensland Government Department of Agriculture and Fisheries, Forest Products Innovation, Salisbury Research Facility, Salisbury, QLD 4107, Australia

Abstract

With the ongoing emphasis on sustainable and eco-friendly construction, there is a rising demand for high-strength and high-stiffness engineered wood products. This trend presents both opportunities and challenges for the Australia's hardwood industry, particularly concerning native forest-grown spotted gum (*Corymbia citriodora*). Glue laminated (glulam) spotted gum beams cannot be confidently commercialised due to the difficulty for its high-density to satisfy the bond integrity criteria (referred to as "delamination test") for external products in accordance with the Australia and New Zealand Standard AS/NZS 1328.1 (1998). To investigate potential solutions for passing this delamination test, an accurate numerical model can be a valuable and time-efficient tool. The aim of this study is to develop and detail such a model, considering heat and mass transfer, drying stresses, plasticity and fracture propagation models, using COMSOL Multiphysics 5.5. The model was validated against a series of wetting and drying experiments on spotted gum glulam, considering both moisture content variation and crack propagation along the gluelines. Results from the validated model showed that delamination is principally due to the tensile stress applied to the gluelines. Through the comprehensive analysis of the moisture content and stress distributions during delamination test, alternative strategies for reducing delamination can be identified.

Keywords: *glued laminated timber, moisture content, fracture, delamination, drying stress*

1. Introduction

Amidst the prevailing push for eco- and environmentally-friendly construction, an increasing demand exists for engineered wood products that provide high-stiffness and high-strength performance. This trend presents both opportunities and challenges for the Australia's hardwood industry, particularly for native forest spotted gum (SPG - *Corymbia citriodora*), which constitutes approximately 70% of annual hardwood harvested logs from Queensland's native forests (Queensland Government Department of Agriculture and Fisheries, 2016). SPG has a high potential to produce high performance engineered wood products due to its high density and superior mechanical performance (Bootle, 1983; Leggate et al., 2022a). One of these products is glue laminated timber (glulam) which consists of boards glued together, allowing large cross-sections to be manufactured (Ross, 2010). Nevertheless, SPG glulam beams cannot be confidently commercialised due to the difficulty in satisfying the glueline bond integrity criteria (commonly referred to as “delamination test”) for external products in accordance with the Australia and New Zealand Standard AS/NZS 1328.1 (1998), a test which involves cycles of vacuum impregnation of water and drying. This difficulty for poor adhesion and subsequent delamination of the gluelines can be summarised in two aspects. First, the material presents (1) poor adhesive penetration, (2) high level of extractive, (3) low wettability and (4) minimal permeability (Leggate et al., 2020; Leggate et al., 2021a; Leggate et al., 2022b; Leggate et al., 2021b). Extensive attempts have been made to enhance its gluability but still no solution was found to produce satisfactory glueline bonds (Leggate et al., 2020; Leggate et al., 2021a; Leggate et al., 2022b; Leggate et al., 2021b). Second, high moisture shrinkage coefficients coupled with high elastic moduli (Guitard & El Amri, 1987; Redman, 2017) likely lead to the formation of significant moisture-induced internal stresses within the adhesive joints during delamination testing. Therefore, if the gluability cannot be improved, mechanically reducing the moisture-induced stresses may address the issue of delamination of SPG glulam. There are various approaches that can be employed to achieve this objective. First, considering the distinct shrinkage and swelling coefficients of the material along its radial and tangential directions (Redman, 2017), arranging the boards in different permutations may decrease the shrinkage difference among board layers and reduce the stresses imposed to the gluelines.

Second, incorporating precisely shaped and strategically arranged stress relief profiles into boards could also alleviate internal stresses (Raftery & Whelan, 2014). Last, altering the board geometry, particularly the width-to-thickness ratio, is anticipated to exert an impact on internal stresses, consequently potentially reducing the stress experienced by the gluelines during the delamination test.

The development of a numerical model through the finite element (FE) modelling method could be an effective way to validate the previous assumptions and investigate mechanical solutions to prevent delamination. However, to the best authors' knowledge, such a model which thoroughly and adequately considers heat and mass transfer, drying stresses, plasticity and fracture propagation along the gluelines does not exist. Redman (2017), Angst and Malo (2010) and Angst (2012) developed models for which the moisture distribution inside the material was first profiled, after which the internal stresses were calculated based on the moisture gradient, and finally, the location of failure was determined based on the stress values. For the moisture distribution, a continuum approach was utilised, and the macroscopic partial differential equations of porous media transport were solved from volume averaging of the microscopic conservation laws (Couture et al., 1996; Whitaker, 1977). For the moisture-induced internal stress, linear constitutive equations (Aicher & Dill-Langer, 1997; Mårtensson, 1994) with no proper plasticity criteria for ductile failure of the material in compression and crack propagation model for brittle failure modes were employed.

The aim of this paper is to develop and present a comprehensive numerical delamination model that considers both the heat and mass transfer and mechanical (elasticity, plasticity and fracture) behaviours of the material during the delamination test in accordance with the AS/NZS 1328.1 (1998). COMSOL Multiphysics version 5.5 (COMSOL Multiphysics, 2019), which is an engineering finite element analysis software that can simulate multiple coupled physics scenarios, was selected as the modelling software. The model was validated against a series of tests performed on SPG glulam for both moisture content variation and the evolution of the delamination of the gluelines. The model was then used to understand the phenomena leading to delamination. The paper is organised as follows: (1) the experimental tests performed to obtain either input values for the model or to validate the model are first presented, (2) the

governing equations of the heat-mass transfer model and validation of the model in one-dimensional (1D) are presented, (3) the mechanical model is introduced and the coupled heat and mass transfer and mechanical model is validated against the three-dimensional (3D) experimental results by Faircloth et al. (2024) and (4) finally, the numerical model is used to provide insight on the delamination process of SPG glulam.

The present study is significant as it represents the first attempt to develop a comprehensive delamination model for high-density hardwood glulam considering couple heat-mass transfer with mechanical model. Based on a fundamental understanding of the delamination process gained from the model, the study seeks to eventually investigate potential solutions to provide satisfactory glueline bonds. As previously mentioned, enabling Australian SPG glulam to be added to the market, would ultimately generate financial benefits to the local timber industry. In addition, by changing the input values, the model can also be applied to other high-density hardwood, or even softwood species, which provide similar challenges to SPG.

Note, this study is limited to the more stringent drying process of the delamination test in the AS/NZS 1328.1 (1998), and the physical and mechanical consequences on the material on the wetting process is outside the scope of this study. However, the moisture content within the glulam after the wetting process was measured experimentally and was used as the initial condition for the drying model.

2. Experimental tests

This section introduces experimental tests which were used to:

- Measure the 1D and 3D moisture content variations within single boards and glulam samples, respectively, after the water impregnation process of the delamination test. These moisture gradients were used as initial input moisture conditions in the FE model. These samples were manufactured and tested as part of this study. The test setups and results are described in Section 2.2.
- Obtain experimental data to validate the model during the drying process of the delamination test in two steps: (1) the heat-and-mass transfer model was first validated

in 1D on drying tests performed on single SPG boards, and (2) the combined heat-and-mass transfer and mechanical model was validated in 3D based on the SPG glulam samples tested in Faircloth et al. (2024).

2.1 Manufactured samples

To obtain the moisture content variation with the timber after water impregnation and validate the drying heat-and-mass transfer model in 1D, 30 native forest SPG boards were milled to 22 mm thick using the process described later in this section for the 3D samples. The final boards had nominal dimensions of 25 mm × 98 mm × 22 mm. For each board, five surfaces were sealed with epoxy, leaving only one surface as an open boundary (having a cross-section of 25 mm × 22 mm) for mass transport. Half of the samples were designed for longitudinal (L) direction moisture movement (with one radial (R) – tangential (T) plane left as the open surface), and the remaining samples were designed for transverse direction moisture movement (with either one RL or TL plane left as the open surface, with no distinction between the two planes).

The 3D samples used to either obtain the 3D moisture gradient after the water impregnation (manufactured as part of this study) or to validate the FE model (manufactured in Faircloth et al. (2024)) followed the requirements in AS/NZS 1328.1 (1998). Especially, four 22 mm thick native forest SPG boards were glued together to form an 88 mm thick glulam, 75 mm long and 85 mm wide. The gluing process was guided by the findings in Leggate et al. (2022b), Leggate et al. (2020) and Leggate et al. (2021a), who aimed at maximising adhesion. This process involved milling the boards to the required thickness to activate their surfaces and utilising a commercial 2-part resorcinol–formaldehyde (RF) adhesive (resin 950.82 and hardener 950.85 from Jowat Adhesives). The specific steps of the gluing process included:

- mixing the resin with the hardener at a ratio of 4:1 for 5 minutes, followed by allowing the mixture to stand for 10 minutes.
- face milling the surfaces intended for bonding in a Rotoles 400 D-S, manufactured by Ledinek.

- manually applying the adhesive to the milled surfaces immediately after milling at a spread rate of 450 grams per square metre (g/m²).
- applying a pressure of 1.4 MPa to press the boards together for 12 hours.

After manufacturing and before testing, all glulam samples and single boards were placed into a conditioning chamber set at 20°C/65% relative humidity until they reached moisture content equilibrium, which consisted of a mass change of less than 0.2% over a 24-hour period (AS/NZS 1080.1, 2012). The actual moisture content of each sample after conditioning was determined following the oven–dry method in AS/NZS 1080.1 (2012), and the average moisture content was found to be 12.5% with a coefficient of variation of 1.96%.

As part of the study, a total of five glulam samples were prepared to measure the moisture gradient after water impregnation. All samples were manufactured from different plain sawn boards.

Results from three glulam samples manufactured in Faircloth et al. (2024), from which relevant data were available, were used for the full 3D model validation. The three manufactured samples had the board orientations shown in Figure 1.

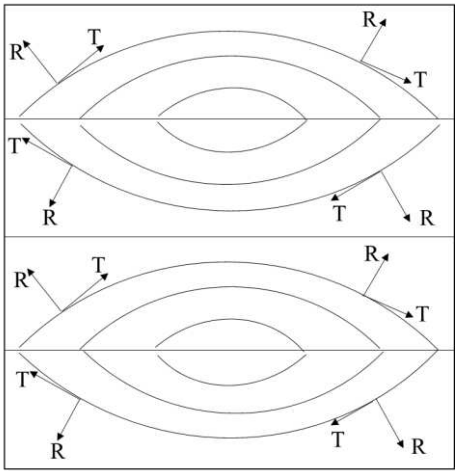

Figure 1. SPG Glulam board permutation in Faircloth et al. (2024), showing the grain directions

2.2 1D and 3D moisture content gradient measurement after water impregnation

2.2.1 Set-up

Method A in appendix C of the AS/NZS 1328.1 (1998) (i.e., for external application) was followed to water impregnate the five 3D glulam samples and the 30 single boards to determine the moisture content gradient after the wetting process of the delamination test.

The specimens were placed inside a pressure vessel and weighed down adequately. Water between 10°C to 20°C was introduced into the vessel ensuring that there was enough water to completely submerge the test samples. Then, the specimens were held by wire screens, ensuring that all surfaces were fully exposed to the water. A 75 kPa vacuum was initiated and maintained for 5 minutes. Then a 550 kPa pressure was applied for a duration of 1 hour. The vacuum-pressure cycle was repeated, ensuring a two-cycle impregnating period totalling 130 minutes. This vacuum-pressure chamber is shown in Figure 2.

Figure 2. Vacuum-impregnation chamber for wetting experiments at the Salisbury Research Facility

Immediately after water impregnation, the moisture content of the SPG samples was measured by a timber moisture metre (manufactured by Deltron Moisture Metres) at the locations shown in Figure 3. For the 3D glulam samples, the positions specified in Figure 3 (b) applied to three surfaces of interest, i.e., one end surface, one side surface and one top surface of cross-sectional dimensions of 88 mm × 85 mm, 88 mm × 75 mm and 85 mm × 75 mm, respectively.

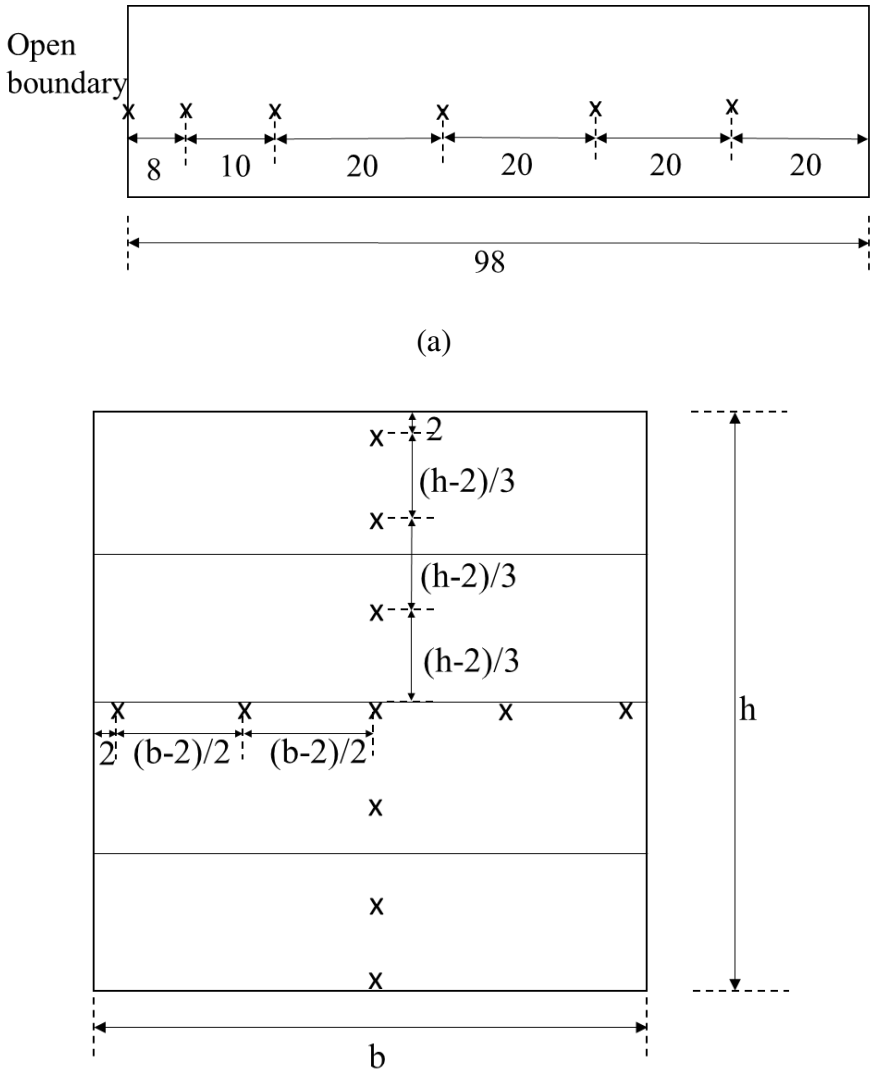

Figure 3. Moisture-metre measuring locations for (a) 1D sawn timber boards and (b) 3D glulam samples (all units in mm)

2.2.2 Results

The average moisture content variations measured along the longitudinal and perpendicular to grain directions on the 1D samples after water impregnation are shown in Figure 4.

Results indicated that the moisture only penetrated approximately 10 mm into the sample, outlining the high non-permeability of the species (Leggate et al., 2022a). Deeper than 10 mm from the open surface, the moisture content was not affected by the vacuum impregnation

process. Therefore, one can be assumed in terms of modelling that only the outer layers, less than 10 mm from the surfaces, absorbed moisture during the wetting process.

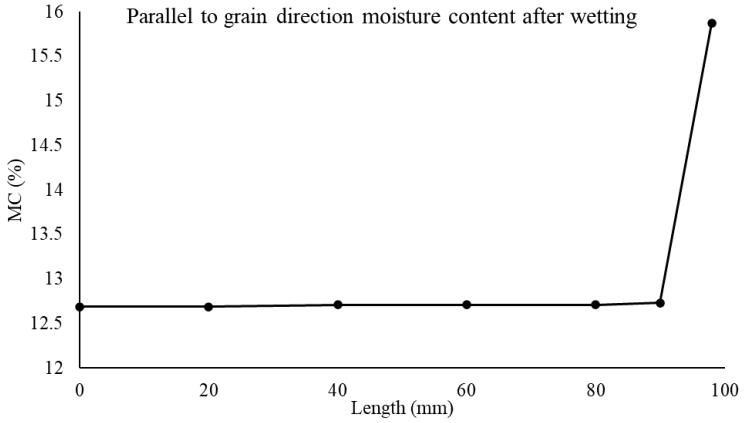

(a)

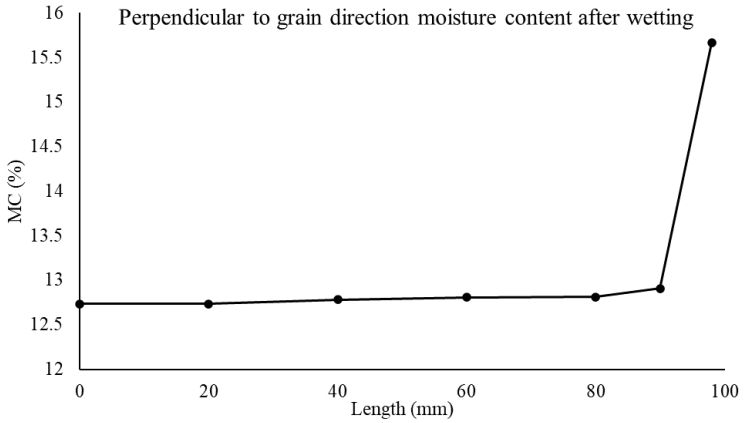

(b)

Figure 4. The moisture content of the 1D samples after the wetting process for (a) parallel to grain and (b) perpendicular to grain directions

The average measured moisture contents at the surface of the 3D SPG glulam are shown in Figure 5, along with the grain directions of the boards. The results are presented for the three surfaces of interest, referred to as Planes A, B and C. The values are in accordance with the 1D samples in Figure 4 and consistent across the three surfaces.

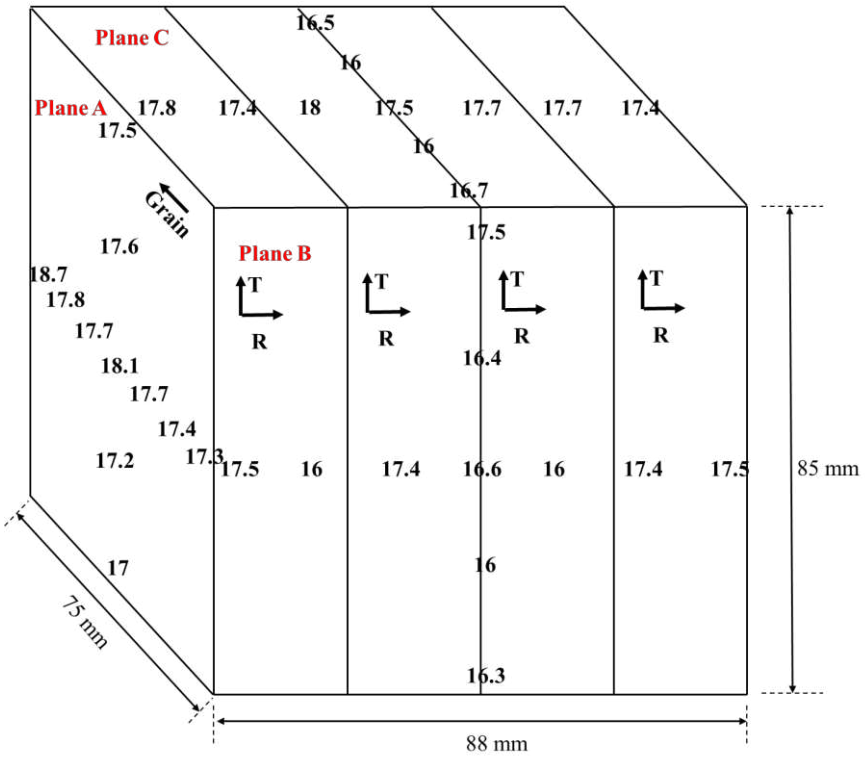

Figure 5. Local moisture content of the SPG glulam for different planes after wetting (values in %)

2.3 1D samples drying tests

2.3.1 Set-up

The 1D SPG single boards used in Section 2.2 were dried following Method A in Appendix C in AS/NZS 1328.1 (1998) immediately after measuring their moisture content. The samples were put into an experimental controlled kiln set to 65°C, a relative humidity of 10% and an air velocity of 2.5 m/s. The drying was conducted over 21 hours with the open surface of the samples exposed to the airflow. High-temperature 1 kN capacity load cells were placed under each sample to measure the weight changes during the kiln drying process. The test setup is shown in Figure 6.

Figure 6. 1D SPG sawn timber drying test setup

After kiln drying, the samples were oven-dried to determine the dry weight from which the actual average moisture content of the samples during the drying process was back calculated.

2.3.2 Results

Figure 7 plots the average moisture content of all 1D SPG samples versus time during the drying process, both for the longitudinal and perpendicular to grain directions. In the initial stage of drying (up to about 3,000 s), the boards dried faster and then reached a steady drying stage to dry to about 11% moisture content after the 21 h cycle. As expected, the transport in longitudinal direction were faster than the transverse direction of the samples. For examples, most the samples reached on average 11.5% moisture content between 10000 s to 40000 s for parallel to grain direction transport whereas it took between 20000 s to 60000 s in perpendicular to grain direction transport.

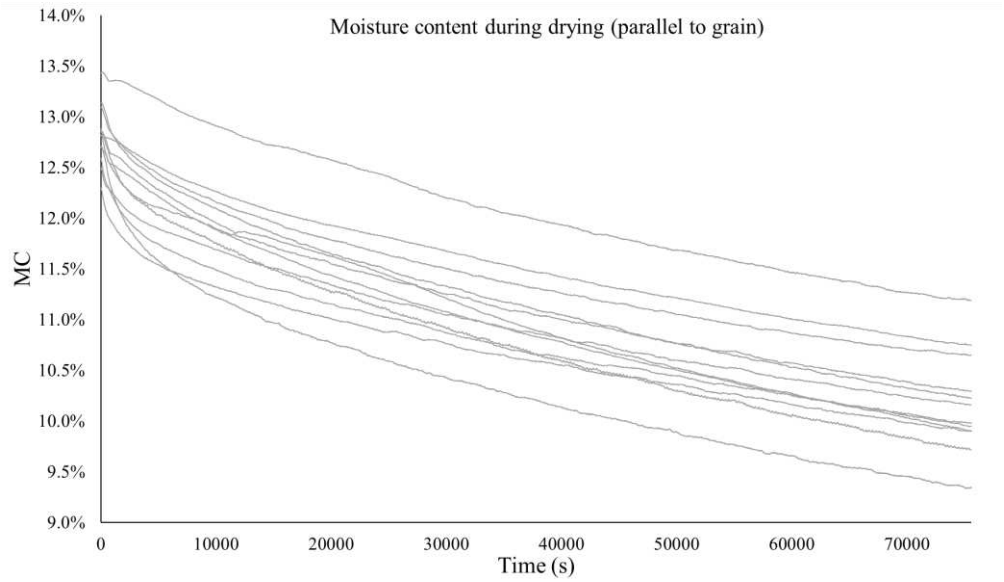

(a)

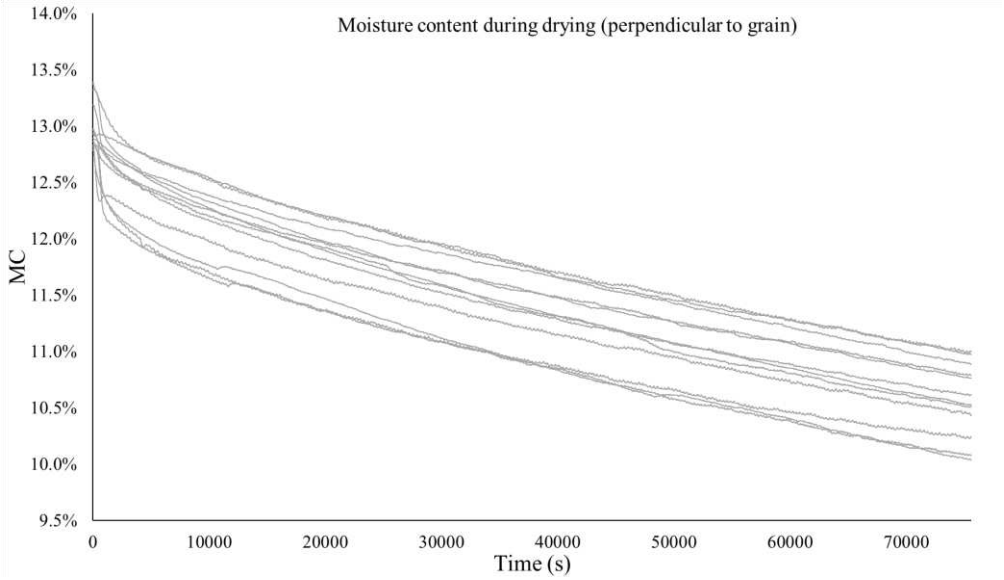

(b)

Figure 7. Results of the 1D SPG samples during drying in (a) the parallel to grain and (b) perpendicular to grain directions

2.4 3D Glulam delamination tests

The three 3D glulam samples in Faircloth et al. (2024) which are used in the paper to validate the FE model were first water impregnated following the methodology and equipment described in Section 2.2.1. The samples were then positioned in a controlled temperature and humidity chamber, fitted with a glass door. A fan was positioned in the chamber to reach the air velocity of 2.5 m/s in the AS/NZS 1328.1 (1998). The chamber was set to the 65^{o}C

temperature and 10% relative humidity stipulated for Method A in Appendix C of the AS/NZS 1328.1 (1998) but was not able to not able to fully match the relative humidity, which was recorded to be 15%.

A black and white speckle pattern was applied to the sample's face facing the glass door, and the evolution of the strain across the speckled surface of the samples was monitored during the 21h of drying using a digital image correlation (DIC) system.

The samples were also individually positioned on a load cell which measured their weight loss. The evolution of the average moisture content of the samples was calculated by measuring the dry weight of each sample using the oven-dry method in the AS/NZS 1080.1 (2012) after the completion of the experiment.

More information on the experimental set-up along with the detailed results can be found in Faircloth et al. (2024).

3. Heat and mass transfer model background

The heat and mass transfer model details moisture transport through an internal porous medium to eventually result in the moisture distribution profile within the material (Whitaker, 1977). Whitaker (1977) proposed mathematical equations for heat and mass transfer modelling, which were proven to be effective and have been widely applied in the drying of timber products (Angst, 2012; Perré, 2007; Redman, 2017; sandoval Torres et al., 2011).

This section details the heat and mass transfer equations as well as input parameters for the FE model simulating the drying process of both 1D and 3D SPG samples.

3.1 General theory and assumptions for heat and mass transfer processes

Wood, as a porous medium, contains three phases of moisture, namely, free water, bound water and water vapour (Whitaker, 1977). The wood fibre saturation point represents the moisture level at which the cell walls are saturated with bound water, while no free water is present in the cell lumina (Ross, 2010). Therefore, below the fibre saturation point, the free water is taken as zero and only bound water is present in the material. Above the fibre saturation point, the

bound water is considered to be a constant and only the free water transports, with interactions between all phases (Gezici-Koç et al., 2017). Practically, the heat and mass transfer phenomena in wood are solved by a continuum approach, and the macroscopic partial differential equations of porous media transport are solved from volume averaging of the microscopic conservation laws (Couture et al., 1996; Whitaker, 1977). The assumptions of heat and mass transfer in wood during drying are given as follows (Couture et al., 1996; Kumar et al., 2016; Turner, 1996):

- The liquid phase is incompressible.
- The continuous gas phase is a perfect mixture of vapour and dry air, which means that the ideal gas law can be applied.
- The solid phase includes an incompressible solid, which is rigid and holds bound water.
- Gravity is excluded for the gas and liquid phases.
- The enthalpy of each phase is a linear function of temperature, and the enthalpy of bound water includes the differential heat of sorption.
- The water vapour is in equilibrium and solely depends on the saturated vapour pressure.
- The capillary pressure is a function of moisture content and temperature.
- All phases are at the same temperature.

3.2 Mathematical definitions and equations for heat and mass transfer processes

This subsection lists the different variables used in the heat and mass transfer equations which are detailed in the following subsections. The different phases are defined herein with the following subscripts: g = gas, v = water vapour, a = air, w = free water, s = solid and b = bound water (Kumar et al., 2016).

According to Ni et al. (1999), the representative elementary volume V from volume averaging of the microscopic conservation laws can be written as:

$$V = V_g + V_w + V_s \tag{1.}$$

where V_i is the volume of phase i.

The porosity φ is defined as the ratio of the wood cell lumen to the woody tissue and is defined as the volume fraction of the pore space (Ni et al., 1999; Perré & Turner, 1999), namely:

$$\varphi = \frac{V_g + V_w}{V} \tag{2.}$$

The free water and gas saturation, which represent the fraction of pore space occupied by free water (S_w) and gas (S_g), are given by Kumar et al. (2016) and Ni et al. (1999) as follows:

$$S_w = \frac{V_w}{V_w + V_g} \tag{3.}$$

$$S_g = \frac{V_g}{V_w + V_g} = 1 - S_w \tag{4.}$$

The volume fractions (ε_i) of the different phases *i* are given by Kumar et al. (2016) and Turner (1996) as:

$$\varepsilon_w = \frac{V_w}{V} = \varphi S_w \tag{5.}$$

$$\varepsilon_g = \frac{V_g}{V} = \varphi S_g \tag{6.}$$

The mass fractions of vapour (ω_v) and air (ω_a) in the gas phase are given by Kumar et al. (2016) and Ni et al. (1999) as follows:

$$\omega_v = \frac{m_v}{m_g} \tag{7.}$$

$$\omega_a = \frac{m_a}{m_g} = 1 - \omega_v \tag{8.}$$

where m_v, m_a and m_g represent the masses of water vapour, air and gas, respectively.

Additionally, the molar fractions of water vapour (χ_v) and air (χ_a) in the gas phase are given by Kumar et al. (2016) as:

$$\chi_v = \frac{\omega_v M_a}{\omega_v M_a + \omega_a M_v} \tag{9.}$$

$$\chi_a = \frac{\omega_a M_v}{\omega_v M_a + \omega_a M_v} \tag{10.}$$

where M_v and M_a represent the molecular weights of water vapour and air, respectively. These values are constant and given in Table 1.

The density ρ_i of phase i is defined as (Kumar et al., 2016):

$$\rho_w = \frac{m_w}{V_w} \tag{11.}$$

$$\rho_g = \frac{m_g}{V_g} = \frac{P_g M_g}{RT} \tag{12.}$$

$$\rho_v = \frac{m_v}{V_g} = \omega_v \rho_g = \frac{P_v M_v}{RT} \tag{13.}$$

$$\rho_a = \frac{m_a}{V_g} = \omega_a \rho_g = \frac{P_a M_a}{RT} \tag{14.}$$

where P_i represents the pressure of phase i, R is the universal gas constant given in Table 1, and T is the porous medium temperature.

The mass concentration c_i of each phase i is given by Turner (1996) as follows:

$$c_w = \frac{m_w}{V} = \varphi S_w \rho_w = \varepsilon_w \rho_w \tag{15.}$$

$$c_g = \frac{m_g}{V} = \varphi S_g \rho_g = \varepsilon_g \rho_g \tag{16.}$$

$$c_v = \frac{m_v}{V} = \varphi S_g \rho_g \omega_v = \varepsilon_g \rho_g \omega_v \tag{17.}$$

$$c_a = \frac{m_a}{V} = \varphi S_g \rho_g \omega_a = \varepsilon_g \rho_g \omega_a \tag{18.}$$

$$c_s = \frac{m_s}{V} = \rho_{dry-wood} \tag{19.}$$

$$c_b = \frac{m_b}{V} \tag{20.}$$

where $\rho_{dry-wood}$ is the dry density of wood and is given in Table 1 for SPG.

3.2.1 Free water conservation equations

The conservation equation of free water is given as (Couture et al., 1996; Kumar et al., 2016; Ni et al., 1999; Perré, 1996; sandoval Torres et al., 2011; Turner, 1996; Whitaker, 1977):

$$\frac{\partial}{\partial t}(c_w) + \nabla \cdot (\overrightarrow{n_w}) = -q_w \qquad (21.)$$

where q_w is the evaporation from free water to vapour and is taken as zero herein as the vapour pressure is considered to be in equilibrium (Seredyński et al., 2020) and $\overrightarrow{n_w}$ is the free water flux given as (Perré & Turner, 2008):

$$\overrightarrow{n_w} = -\rho_w \frac{k_w \times K_w}{\mu_w} \nabla(P_g - P_c) \qquad (22.)$$

where k_w is the relative permeability of water, K_w is the absolute permeability of water, μ_w is the dynamic viscosity of water, P_c is the capillary pressure, and P_g is the gas pressure solved by the gas conservation equation (Kumar et al., 2016):

$$\frac{\partial}{\partial t}(c_g) + \nabla \cdot \left(-\frac{\rho_g \times k_g \times K_g}{\mu_g} \nabla P_g \right) = q_b + q_w \qquad (23.)$$

where k_g is the relative permeability of gas, K_g is the absolute permeability of gas, μ_g is the dynamic viscosity of gas, and q_b is the evaporation from bound water to vapour and is taken as zero herein as the vapour pressure is considered to be in equilibrium (Seredyński et al., 2020).

The values of all the parameters in the free water and gas conservation Equations (21) to (23) are given in Table 1.

3.2.2 Bound water conservation equations

The conservation equation of bound water is given as (Couture et al., 1996; Perré, 1996; sandoval Torres et al., 2011; Turner, 1996; Whitaker, 1977):

$$\frac{\partial}{\partial t}(c_b) + \nabla \cdot (\overrightarrow{n_b}) = q_b \qquad (24.)$$

where $\overrightarrow{n_b}$ is the bound water flux given as (Couture et al., 1996):

$$\overrightarrow{n_b} = -D_b \cdot \nabla c_b \quad (25.)$$

where D_b is the bound water diffusion coefficient.

The values of all the parameters in the bound water conservation Equations (24) and (25) are given in Table 1.

3.2.3 Water vapour conservation equations

The conservation equation of water vapour is given as (Couture et al., 1996; Kumar et al., 2016; Ni et al., 1999; Perré, 1996; sandoval Torres et al., 2011; Turner, 1996; Whitaker, 1977):

$$\frac{\partial}{\partial t}(c_v) + \nabla \cdot (\overrightarrow{n_v}) = q_w + q_b \quad (26.)$$

where $\overrightarrow{n_v}$ is the water vapour flux:

$$\overrightarrow{n_v} = -\frac{\rho_v \times k_g \times K_g}{\mu_g} \nabla P_g - \rho_g D_{eff} \nabla \omega_v \quad (27.)$$

where D_{eff} is the effective diffusivity of gas.

The values of all the parameters in water vapour conservation Equations (26) and (27) are given in Table 1.

3.2.4 Air conservation equations

The conservation equation of air is given as (Couture et al., 1996; Perré & Turner, 1999; Turner, 1996):

$$\frac{\partial}{\partial t}(c_a) + \nabla \cdot (\overrightarrow{n_a}) = 0 \quad (28.)$$

where $\overrightarrow{n_a}$ is the air flux:

$$\overrightarrow{n_a} = -\frac{\rho_a \times k_g \times K_g}{\mu_g} \nabla P_g - \rho_g D_{eff} \nabla \omega_a \quad (29.)$$

The air conservation equation does not need to be programmed, as it is intrinsic to Equations (25) and (28). They are given in the paper in the sake of providing all relevant equations.

3.2.5 Energy conservation equations

The heat transfer is governed by the energy conservation equation, given as (Couture et al., 1996; Turner, 1996; Whitaker, 1977):

$$\frac{\partial}{\partial t}\left(c_s h_s + c_a h_a + c_v h_v + c_w h_w + c_b \bar{h}_b\right) + \nabla \cdot \left(h_w \overrightarrow{n_w} + h_a \overrightarrow{n_a} + h_v \overrightarrow{n_v} + h_b \overrightarrow{n_b}\right) = \nabla \cdot \left(\bar{\lambda}_{eff} \nabla \mathrm{T}\right) \quad (30.)$$

where h_i is the enthalpy of phase i, $\overrightarrow{n_i}$ is the flux of phase i, and $\bar{\lambda}_{eff}$ is the effective thermal conductivity of the material.

The enthalpy of each phase is given as (Couture et al., 1996; Turner, 1996):

$$h_s = C_{p_s}(T - T_R) \quad (31.)$$

$$h_w = C_{p_w}(T - T_R) \quad (32.)$$

$$h_a = C_{p_a}(T - T_R) \quad (33.)$$

$$h_v = C_{p_v}(T - T_R) + h_{evap}^0 \quad (34.)$$

$$h_b = h_w - \Delta H \quad (35.)$$

$$\bar{h}_b = h_w - \frac{1}{c_b}\int_0^{c_b} \Delta H \, dp \quad (36.)$$

where C_{p_i} is the specific heat of phase i, T_R is the reference temperature, h_{evap}^0 is the latent heat at the reference temperature. ΔH is the heat of sorption, given as (Turner, 1996):

$$\Delta H = 0.4 h_{evap}\left(1 - \frac{c_b}{c_{fsp}}\right)^2 \quad (37.)$$

where h_{evap} is the latent heat of evaporation, c_{fsp} is the mass concentration of moisture at the fibre saturation point.

Substituting Equations (31) – (37) into Equation (30), one obtains the equation to be imported into COMSOL Multiphysics in the form:

$$\left(\rho C_p\right)_{eff}\frac{\partial T}{\partial t}+\nabla \mathrm{T}\left(C_{p_a}\overrightarrow{n_a}+C_{p_v}\overrightarrow{n_v}+C_{p_w}(\overrightarrow{n_w}+\overrightarrow{n_b})\right)$$
$$-0.4h_{evap}\frac{\partial}{\partial t}\left(c_b\left(1-\frac{c_b}{c_{fsp}}+\frac{1}{3}\left(\frac{c_b}{c_{fsp}}\right)^2\right)\right)-0.4h_{evap}\nabla\cdot\left(\overrightarrow{n_b}\left(1-\frac{c_b}{c_{fsp}}\right)^2\right)$$
$$=\nabla\cdot\left(\bar{\lambda}_{eff}\nabla \mathrm{T}\right) \quad (38.)$$

where

$$\left(\rho C_p\right)_{eff}=c_s C_{p_s}+c_a C_{p_a}+c_v C_{p_v}+(c_w+c_b)C_{p_w} \quad (39.)$$

$$\bar{\lambda}_{eff}=\varepsilon_w\lambda_w+\varepsilon_s\lambda_s+\varepsilon_v\lambda_v+\varepsilon_a\lambda_a+\varepsilon_b\lambda_b \quad (40.)$$

The values of all the parameters in heat conservation Equations (30) - (40) are given in Table 1.

3.2.6 Boundary conditions

According to Couture et al. (1996), the total moisture mass flux (Q_m) and total heat flux (Q_h) at the boundaries are defined as follows:

$$Q_m=h_m\left(\rho_v-\rho_{vinf}\right) \quad (41.)$$

$$Q_h=h_h\left(T-T_{inf}\right) \quad (42.)$$

where h_m is the mass transfer coefficient; h_h is the heat transfer coefficient; ρ_{vinf} is the vapour density at an infinite position (i.e., the vapour density in the surrounding environment); and T_{inf} is the temperature at an infinite position.

Kumar et al. (2014) rewrote Equation (41) by considering the boundary conditions individually for the free water, water vapour and bound water as follows:

For free water:

$$\overrightarrow{n_w} \cdot \hat{n} = h_m \varepsilon_w \frac{(P_v - P_{air})}{RT} \quad (43.)$$

For water vapour:

$$\overrightarrow{n_v} \cdot \hat{n} = h_m \varepsilon_g \frac{(P_v - P_{air})}{RT} \quad (44.)$$

For bound water:

$$\overrightarrow{n_b} \cdot \hat{n} = h_m (1 - \varphi) \frac{(P_v - P_{air})}{RT} \quad (45.)$$

where $\hat{n}$ is the exterior normal unit vector and P_{air} is the pressure of the surrounding air.

The mass transfer coefficient h_m is taken from Redman (2017) and given as follows:

$$h_m = \frac{h_h}{\rho_a C_{p_a}} \quad (46.)$$

The heat transfer coefficients in the previous equations proposed by Perussello et al. (2014) and Bird (2002) are used in this study and given as follows:

$$h_h = 0.683 \frac{\lambda_a}{L} (Pr)^{0.33} (Re)^{0.466} \quad (47.)$$

where L is the characteristic length of the drying sample, taken as half of the sample width; Pr and Re are the Prandtl number and Reynolds number, respectively, determined as follows:

$$Pr = \frac{C_{p_a} \mu_a}{\lambda_a} \quad (48.)$$

$$Re = \frac{\rho_a v_a L}{\mu_a} \quad (49.)$$

where v_a is the air velocity.

By substituting Equation (48) and Equation (49) into Equation (47), the heat transfer coefficient can be calculated.

3.2.7 Initial moisture conditions

From the results presented in Section 2.2.2, the moisture content in the SPG samples after the water impregnation stage was ideally modelled to decrease linearly from the surface to a depth of 10 mm and that the moisture content in the core parts of the samples (i.e., deeper than 10 mm from the surface) is equal to the moisture resulting from the initial conditioning (i.e., measured at 12.5%). Consequently, for the 1D single boards samples, the initial moisture content in the samples were inputted for the experimental data shown in Figure 4. The moisture content inside the specimen was set to 12.5% and increased linearly from 10 mm away from the surface to 15.87% and 15.66% at the surface in the longitudinal and perpendicular to grain directions, respectively. A similar approach was followed for the 3D SPG glulam samples, with the moisture content deeper than 10 mm from the surfaces equal to 12.5% and increasing linearly from a depth of 10 mm to the surfaces. The moisture contents at the end, top and side surfaces were taken from the experimental data as 16.78%, 17.64% and 17.18%, respectively.

Table 1. Heat and mass transfer model parameters used in SPG drying model

Parameter	Description	Value	Unit	Reference
ρ_w	Free water density	10^3	*kg/m³*	
$\rho_{dry-wood}$	Dry wood density	921	*kg/m³*	Redman (2017)
W_{fsp}	Fibre saturation point	24	*%*	Redman (2017)
R	Universal gas constant	8.3144	*J/K/mol*	
M_a	Molecular weight of air	28.966	*g/mol*	Çengel and Boles (2006)
M_w; M_v	Molecular weight of water and vapour	18.016	*g/mol*	
M_g	Molecular weight of gas	$M_g = \chi_v \times M_v + (1 - \chi_v) \times M_a$	*g/mol*	Kumar et al. (2016)
K_w^R; K_g^R	Absolute permeability of water and gas in radial direction	0.01×10^{-20}	*m²*	Redman et al. (2012)
K_w^L; K_g^L	Absolute permeability of water and gas in longitudinal direction	0.08×10^{-15}	*m²*	
K_w^T; K_g^T	Absolute permeability of water and gas in tangential direction	0.35×10^{-20}	*m²*	
D_b^T; D_b^R	Bound water diffusivity in radial and tangential direction	0.14×10^{-10}	*m²/s*	
D_b^L	Bound water diffusivity in longitudinal direction	0.6×10^{-10}	*m²/s*	
c_1	Desorption-isotherm parameter	1.0047		Redman et al. (2016)

c_2	Desorption-isotherm parameter	0.9076		
C_{p_w}	Specific heat of water	4183	*J/kg/K*	Carr et al. (2013)
C_{p_v}	Specific heat of vapour	1900	*J/kg/K*	
C_{p_a}	Specific heat of air	1006	*J/kg/K*	
C_{p_s}	Specific heat of hardwood	1400	*J/kg/K*	Redman (2017)
h_{evap}	Latent heat of evaporation	2.26×10^6	*J/kg*	Çengel and Boles (2006)
λ_v	Thermal conductivity of water vapour	0.023	*W/m/K*	Perré and Turner (2001)
λ_a	Thermal conductivity of air	0.023	*W/m/K*	
λ_w	Thermal conductivity of free water	0.5	*W/m/K*	
λ_b	Thermal conductivity of bound water	0.5	*W/m/K*	
λ_s	Thermal conductivity of hardwood	1.9	*W/m/K*	MacLean (1941)
μ_w	Dynamic viscosity of water	$\mu_w = \rho_w e^{(-19.143+\frac{1540}{T})}$	*Pa*s*	Kumar et al. (2016)
μ_a	Dynamic viscosity of air	$\mu_a = 0.59 \times 10^{-5} + 4.2 \times 10^{-8} T$	*Pa*s*	Bird (2002)
μ_v	Dynamic viscosity of vapour	$\mu_v = -3.189 \times 10^{-6} + 4.145 \times 10^{-8} T + -8.272 \times 10^{-13} T^2$	*Pa*s*	
μ_g	Dynamic viscosity of gas	$\mu_g = \frac{P_a \mu_a \sqrt{M_a} + P_v \mu_v \sqrt{M_v}}{P_a \sqrt{M_a} + P_v \sqrt{M_v}}$	*Pa*s*	
k_w^R	Relative permeability of water in radial direction	$k_w^R = (S_w)^3$		Perré and Turner (1999)
k_w^L	Relative permeability of water in longitudinal direction	$k_w^L = (S_w)^8$		

$k_g^T;\ k_g^R$	Relative permeability of gas in radial and tangential direction	$k_g^T = 1 + (2S_w - 3)(S_w)^2$		
k_g^L	Relative permeability of gas in longitudinal direction	$k_g^L = 1 + (4S_w - 5)(S_w)^4$		
P_c	Capillary pressure	$P_c = 1.24 \times 10^5 \times (77.5 - 0.185T) \times 10^{-3} \times (S_w + 1 \times 10^{-4})^{-0.61}$	*Pa*	Turner and Perré (2004)
P_{vs}	Saturation vapour pressure	$P_{vs} = \exp\left[-\frac{5800.2206}{T} + 1.3915 - 0.0486T + 0.4176 \times 10^{-4} \times T^2 \quad 0.01445 \times 10^{-7} \times T^3 + 6.656\ln(T)\right.$	*Pa*	Vega-Mercado et al. (2001)
P_v	Partial pressure of vapour	$P_v = 1 - \exp(-C_1 A - C_2 A^2) \times P_{vs}$ with $A = \frac{W_b}{(W_{fsp} - \frac{0.1 W_{fsp}}{32.5} T)}$	*Pa*	Perré and Turner (1999)
D_v	Mass diffusivity of vapour in the air	$D_v = 2.2 \times 10^{-5}(\frac{1.013 \times 10^5}{P_v})(\frac{T}{273})^{1.75}$	m^2/s	Dymond (1999)
D_{eff}^T	Gaseous diffusion in radial direction	$D_{eff}^T = 10^{-5} \times k_{rg}^T \times D_v$	m^2/s	Perré and Turner (1999); Redman (2017)
D_{eff}^R	Gaseous diffusion in tangential direction	$D_{eff}^R = 2 \times 10^{-2} \times D_{eff}^T$	m^2/s	
D_{eff}^L	Gaseous diffusion in longitudinal direction	$D_{eff}^L = D_{eff}^T$	m^2/s	
c_{fsp}	Mass concentration of moisture at the fibre saturation point	$c_{fsp} = W_{fsp} \times \rho_{dry-wood}$	kg/m^3	

4. Heat and mass transfer model validation in 1D

4.1 1D FEM for heat and mass transfer

The 1D SPG single boards used in the drying experiments (Section 2.3.2) were modelled for longitudinal and transverse moisture movement to first validate in 1D the heat and mass transfer equations and inputs presented above. The additional validation of the model in 3D, and based on the tests conducted by Faircloth et al. (2024), is performed in Section 2.4.

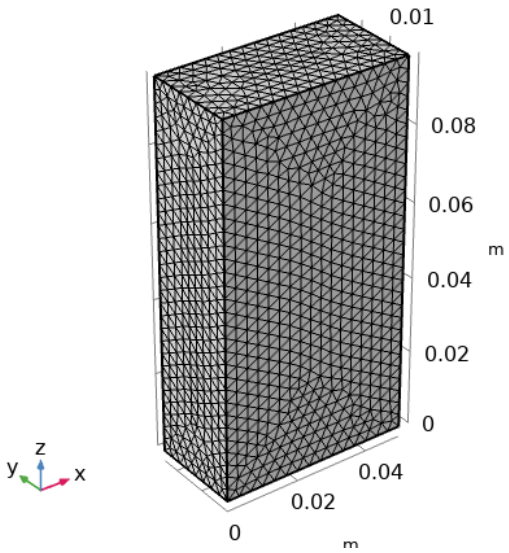

Figure 8. The geometry of the SPG single boards heat and mass transfer model in 1D

A 3D FE model was generated in COMSOL Multiphysics 5.5 with its geometry and mesh shown in Figure 8. The mesh size, with elements with sides of about 3 mm, was found to provide a good compromise between accuracy and computational time. The Coefficient Form Partial Differential Equation physics in COMSOL Multiphysics was selected to describe the conservation equations for heat and mass transfer. Results from the water impregnation in Section 2.2.2 showed that the moisture content in the material was below the fibre saturation point. Therefore, theoretically, the water is only present in the form of bound water (Gezici-Koç et al., 2017), significantly simplifying the equations presented in Section 3.2. However, due to the nature of the water impregnation test, designed to replace the air in the cell lumens with water (i.e., in the form of free water), and the high non permeability of the material, it is unclear whether there was enough time for the absorbed water to be transformed into bound water or if it was still present in the form of free water. Therefore, the model was run twice, once considering all water to be bound water and a second time considering the water absorbed

during the water impregnation process as free water and the water already present in the material before the impregnation process as bound water.

In addition, the initial temperature of the SPG samples at the beginning of the drying stage was assumed to equal to the outdoor temperature of 20°C. The boundary conditions are described by Equations (42), (43), (44) and (45) for heat, free water, water vapour and bound water, respectively, relative to the kiln conditions given in Section 2.3.1.

4.2 Model validation (results)

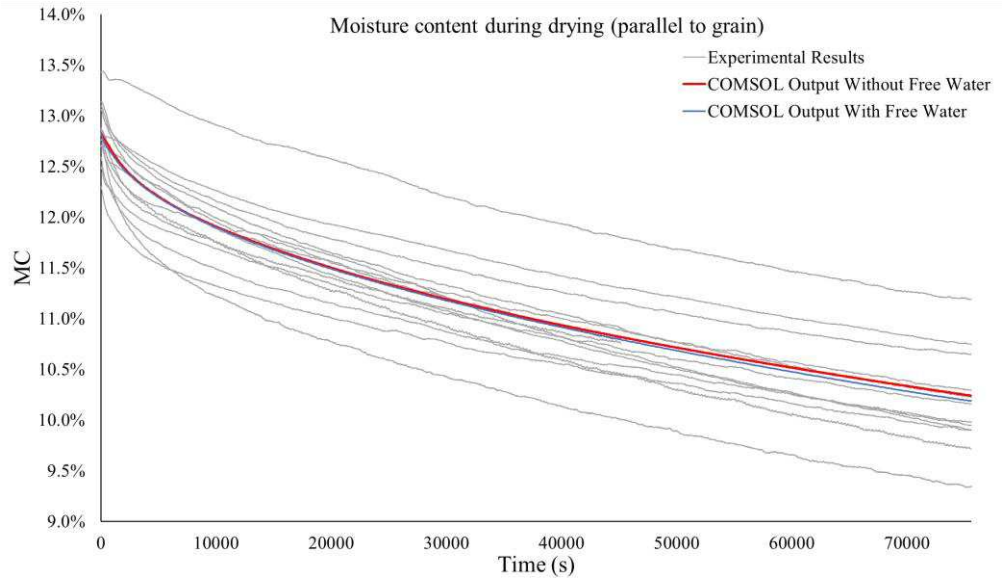

(a)

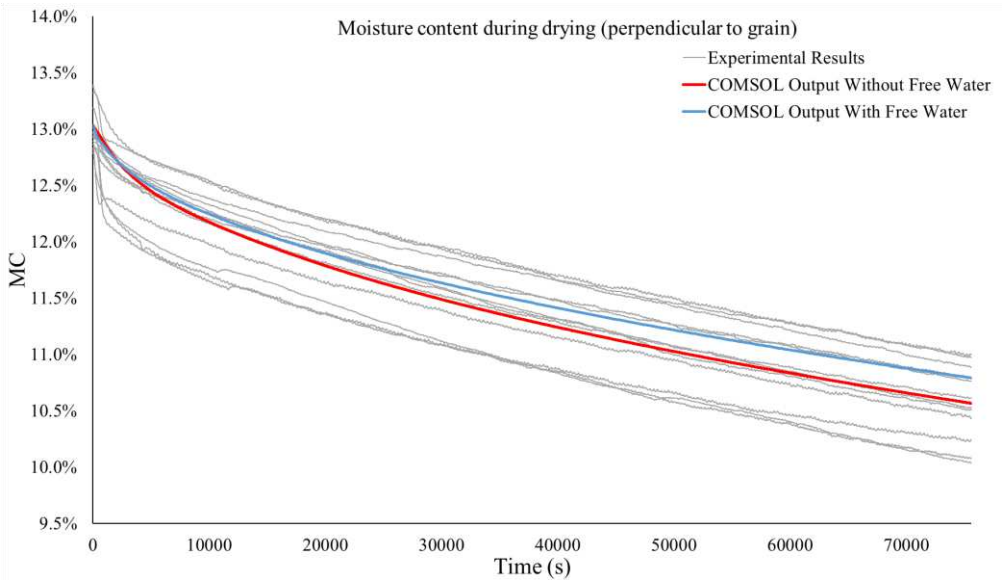

(b)

Figure 9. FE outputs and experimental results for the heat and mass transfer of the SPG sawn timber in the (a). longitudinal and (b). perpendicular to grain directions

Figure 9 compares the experimental to the numerical results for the SPG single boards subjected to 1D drying in the longitudinal and perpendicular to grain directions. For both the models with and without considering free water, the moisture content decreased with increasing drying time, with the model outputs well correlated with the experimental results. In addition, the models with or without considering the free water show no significant difference in the longitudinal direction. However, the model without considering the free water better matches the experimental tests in the perpendicular to the grain direction. Therefore, as considering free water significantly increases the computing time due to the added complexity of the heat and mass transfer model, it was decided in this study to consider all water as bound water in all further simulations presented in the paper.

5. Mechanical model background

5.1 General theory and assumptions for the mechanical model

When wood loses moisture during the drying process, it experiences shrinkage. Also during drying, as a moisture gradient is present in the material, it does not shrink uniformly leading internal drying stresses. Once the moisture-induced internal stresses are too high, either (1) cracks can initiate and propagate, both within the material itself and along the gluelines or (2) the material in compression can plasticise. Therefore, to correctly represent the moisture-induced internal stresses and the underlying delamination process encountered by SPG glulam during the bond integrity assessment in the AS/NZS 1328.1 (1998), both plasticity and fracture mechanics criteria must be considered in the mechanical model.

The drying strains and failure models used as part of this study are described hereafter and coupled with the heat and mass transfer model developed in Section 3 to form a comprehensive glulam delamination analysis model. Validation of this coupled model based on the results in Faircloth et al. (2024) are presented at Section 6.

5.2 Mathematical equations for drying strains

The commonly used constitutive equation of drying strains defined by Mårtensson (1994), Aicher and Dill-Langer (1997), and Hanhijärvi (2000) was applied in this study. The hygro-mechanical model is defined as:

$$\varepsilon = \varepsilon_e + \varepsilon_s + \varepsilon_{ms} + \varepsilon_c \qquad (50.)$$

where ε is the total strain, ε_e is the elastic strain, ε_s is the linear shrinkage-swelling strain, ε_{ms} is the mechano-sorptive creep strain and ε_c is the time-dependent creep strain.

5.2.1 Elastic strain

The constitutive equation of elastic behaviour is described by the Hooke's law (Dahlblom et al., 1996):

$$\varepsilon_e = \boldsymbol{C}\sigma \tag{51.}$$

where σ is the stress vector and $\boldsymbol{C}$ is the compliance matrix.

According to Ross (2010), the mechanical properties of wood vary with respect to the moisture content, and this approach was followed in this study for the elastic properties of the compliance matrix. Guitard and El Amri (1987) proposed the following equation that describes timber mechanical properties relationship to moisture content *W*.

$$P = \begin{cases} P = P_{12}\left(\frac{P_{12}}{P_{fsp}}\right)^{\left(\frac{12-W}{W_{fsp}-12}\right)} & ,if\ 0 \le W < W_{fsp} \\ P_{fsp} & ,if\ W \ge W_{fsp} \end{cases} \tag{52.}$$

where P is the elastic or shear modulus at moisture content W, P_{12} is the modulus at 12% moisture content, P_{fsp} is the modulus at the fibre saturation point, and W_{fsp} is the moisture content at the fibre saturation point.

The elastic moduli, shear moduli and Poisson's ratios at 12% and fibre saturated point to be inputted in the compliance matrix for the SPG material are taken from Redman (2017), Redman et al. (2011) and Redman et al. (2018) and are shown in Table 2. The properties at any other moisture content were calculated by Equation (52).

Table 2. Elastic properties of SPG at 12% moisture content and fibre saturation point from Redman (2017)

Moisture content (%)	Elastic moduli (GPa)			Shear moduli (GPa)			Poisson's ratios		
	E_R	E_T	E_L	G_{LR}	G_{LT}	G_{RT}	v_{RT}	v_{LR}	v_{LT}
24.5 (fsp)	2.1	1.4	19.9	1.6	1.3	0.5	0.64	0.41	0.45
12	3.2	2.2	22.7	2.0	1.7	0.8			

5.2.2 Linear shrinkage-swelling strain

The linear shrinkage-swelling strain is induced by the moisture change rate below the fibre saturation point and is solely linked to the change in bound water (Skaar, 2012). The equation is given in the form of:

$$\varepsilon_s = \begin{pmatrix} \alpha(W - W_{fsp}), & if\ W \leq W_{fsp} \\ 0, & if\ W > W_{fsp} \end{pmatrix} \quad (53.)$$

where α is the shrinkage coefficient vector which were measured by Redman et al. (2011) for SPG in the L, R and T directions as follows:

$$\alpha_L = 0.001;\ \alpha_R = 0.374;\ \alpha_T = 0.385$$

5.2.3 Mechano-sorptive creep strain

Changes in moisture under load induces mechano-sorptive creep, i.e., the ability of the material to creep under stress and change of moisture. Different models have been proposed for describing this phenomenon (Hanhijärvi, 1999). The two most widely used are the Kelvin and the Maxwell type models (Hanhijärvi, 1999). The main difference between the two type models is that the former cannot describe the unloading process, and the recovery cannot be modelled (Angst & Malo, 2010). However, as in this study there was no unloading process, the recovery could be disregarded. Therefore, the Maxwell type model was selected for its simplicity. The most widely used Maxwell type model can be found in Salin (1992), Ranta-Maunus (1993), Hanhijärvi (2000) and Ormarsson (1999) and is given as:

$$\varepsilon_{ms} = m\sigma|\dot{W}| \quad (54.)$$

where m is the mechano-sorptive coefficient, while not available for SPG, it is available for Spruce in Ormarsson (1999), and $\dot{W}$ is the moisture content variation with respect to time.

The stresses induced by the mechano-sorptive creep were calculated based on the available parameters for Spruce. It was found that the resulting stresses were significantly smaller than the elastic strain and shrinkage–swelling stresses. As a result, mechano-sorptive creep was disregarded in this study. This approach was also followed by Redman et al. (2018).

5.2.4 Viscoelastic creep strain

Viscoelastic creep is known as the time-dependent creep. Pang (2001) defined the equation to calculate the viscoelastic creep strain in wood as:

$$\varepsilon_c = a.b.\boldsymbol{C}.\sigma.\frac{t_h^{b-1}}{3600} \quad (55.)$$

where a, b are constants, $\boldsymbol{C}$ is the compliance matrix, and t_h is the elapsed time.

For short duration drying problems, the time-dependent creep is small compared with that of mechano-sorptive creep (Toratti & Svensson, 2000). Time-dependent creep is often neglected in drying stress studies (Redman et al. (2018); Toratti and Svensson (2000); Ormarsson et al. (1998)) and was also was disregarded in this study.

5.3 Failure criteria

5.3.1 Crack initiation and propagation

A cohesive zone model approach was followed herein to model the crack initiation and propagation along the gluelines. This approach has been used by many researchers in timber engineering, such as Franke and Quenneville (2011), Cheng et al. (2022) and Gilbert et al. (2020). The cohesive zone approach requires crack locations to be predefined in the model. In this study, cracks were only considered along the gluelines and were modelled as contact pairs in COMSOL Multiphysics. The displacement-based damage model was used in COMSOL Multiphysics to model the crack initiation and propagation.

The fracture criterion selected in COMSOL Multiphysics is defined as follows:

$$\frac{G_I}{G_{IC}} + \frac{G_{II}}{G_{IIC}} = 1 \quad (56.)$$

where G_I and G_{II} represent the work performed along the crack's perpendicular path and the shear directions, respectively, and G_{IC} and G_{IIC} denote the critical fracture energies in these directions. Lu et al. (2023) measured the fracture properties of the SPG material itself and of the SPG gluelines. The glueline fracture parameters extracted from Lu et al. (2023) for the cohesive zone model are listed in Table 3.

Table 3. Fracture properties of gluelines from Lu et al. (2023)

Fracture Mode	Fracture energy (N/mm)	Crack initiation stress (MPa)
Mode I	0.48	6.8
Mode II	2.5	7.4

5.3.2 Quadratic plasticity model

An elastic-perfectly plastic material was considered as part of this study. The quadratic failure criteria approach was followed herein to model the plasticity of the timber. Plasticity was only considered in the directions perpendicular to the grain experiencing the high dimensional changes in the drying process. The criteria adapted from Aicher and Klöck (2001) is as follows:

$$\left(\frac{\sigma_R}{f_R}\right)^2 + \left(\frac{\sigma_T}{f_T}\right)^2 + \left(\frac{\tau_{RT}}{f_{RT}}\right)^2 = 1 \qquad (57.)$$

where σ_R, σ_T and τ_{RT} are the stresses in the R and T directions and the rolling shear stress, respectively, and f_R, f_T and f_{RT} are the compressive strengths in the R and T directions and the rolling shear strength, respectively. The compressive strength in the radial and tangential directions of the SPG can be found from Redman (2017), and the rolling shear strength can be found in Ross (2010) for similar species. The values are provided in Table 4.

Table 4. SPG strength data used for the plasticity model

Parameters	f_R	f_T	f_{RT}
Value	11.9 MPa	11.9 MPa	2.8 MPa

6. Heat and mass and mechanical model validation in 3D

6.1 3D coupled heat and mass and mechanical model

The 1D validated heat and mass transfer model was combined with the mechanical model described earlier to model the drying of the 3D SPG glulam according to the Method A bond integrity test in Appendix C of AS/NZS 1328.1 (1998). As previously mentioned, the model is validated in this section against the delamination tests performed by Faircloth et al. (2024) and summarised in Section 2.4. The initial internal stresses generated during the wetting process were ignored. The mechanical boundary conditions, geometry and mesh of the model is shown

in Figure 10. The mesh, with elements with a side of about 6-7 mm, was found to provide in 3D a good compromise between accuracy and computational time.

The initial moisture gradient applied to the model after the SPG glulam wetting test results is explained in Section 3.2.7. All the outer surfaces were set as open boundaries for the heat and mass transfer process. All heat and mass transfer parameters were taken from Table 1.

The physics of solid mechanics with a non-linear time-dependent solver in COMSOL Multiphysics 5.5 was selected to solve the drying internal stresses and failure of the material. The specimen, board dimensions and orientations, were the same as those of the tested specimens in Faircloth et al. (2024) (Figure 1). The input parameters for fracture mechanics and plasticity can be found in Table 3 and Table 4, respectively.

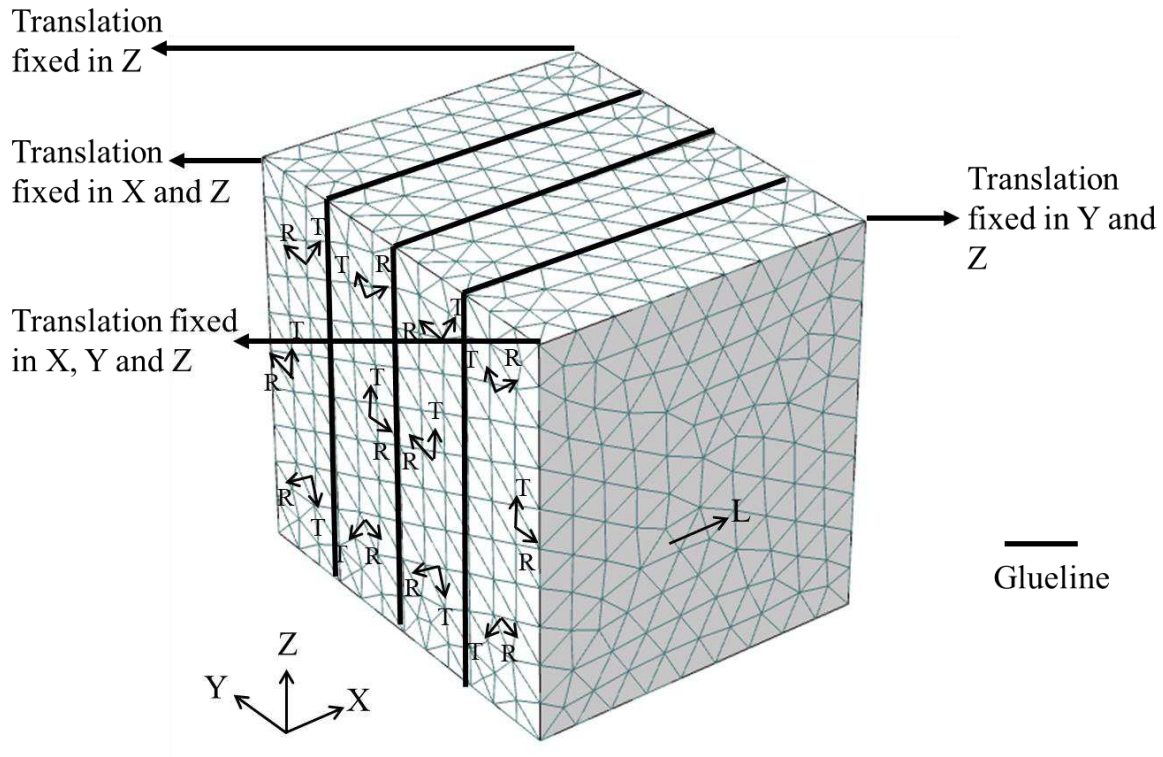

Figure 10. SPG glulam geometry in COMSOL Multiphysics

6.2 Model validation (results)

The average moisture content of the 3D glulam samples extracted from the FE output is compared with the experimental results by Faircloth et al. (2024) in Figure 11 over the 21 h of drying. The numerical simulation results correlate well with the experimental results for

moisture content changes, which further confirms the 3D accuracy of the proposed heat and mass model.

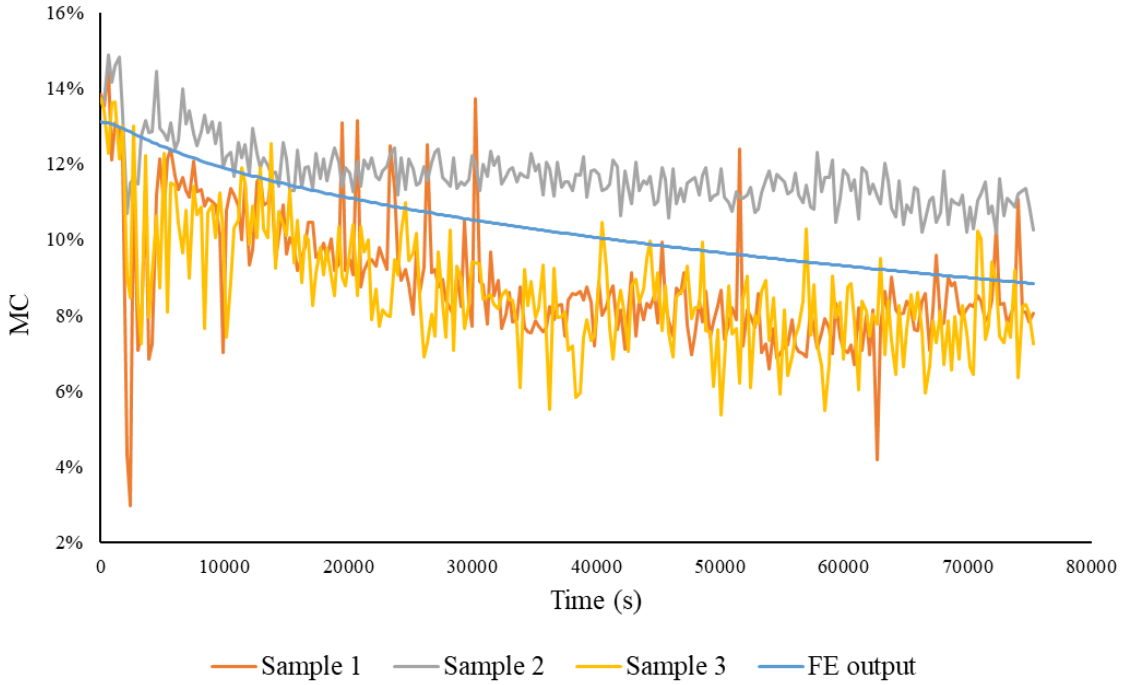

Figure 11. Experimental and numerical comparison of the average moisture content variation for the 3D SPG glulam samples

The data from the DIC were used in this study to extract the opening (delamination) of the gluelines versus time at the locations shown in Figure 12 by using nine virtual extensometers. The results from the DIC extensometers are compared in Figure 13 to the numerical results obtained from extensometers positioned at the same locations in the model. The FE output is strongly correlated with the experimental results for all extensometers. The gluelines typically start to delaminate between 6300 s to 9000 s, as shown by the sudden change in the extensometer reading. This change is well captured by the FE model. The steady crack propagation is also well captured by the FE model for all gluelines. As a result, the proposed model can accurately simulate the delamination process of the SPG glulam material during the bond integrity test.

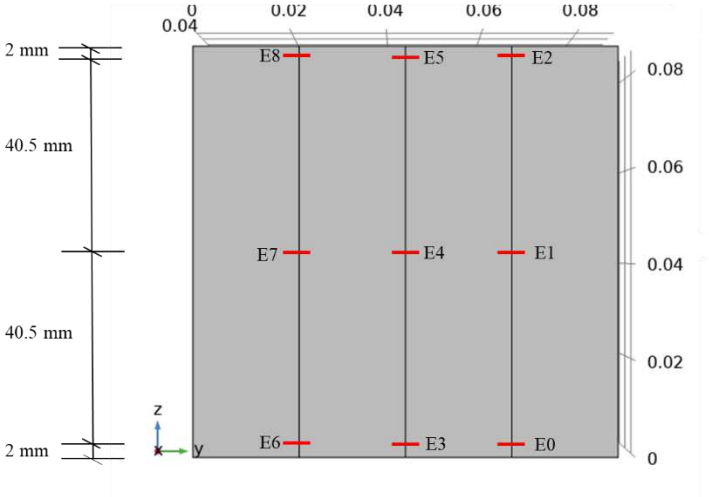

Figure 12. Location of the extensometers positioned on the samples, with extensometers numbered E0 to E8.

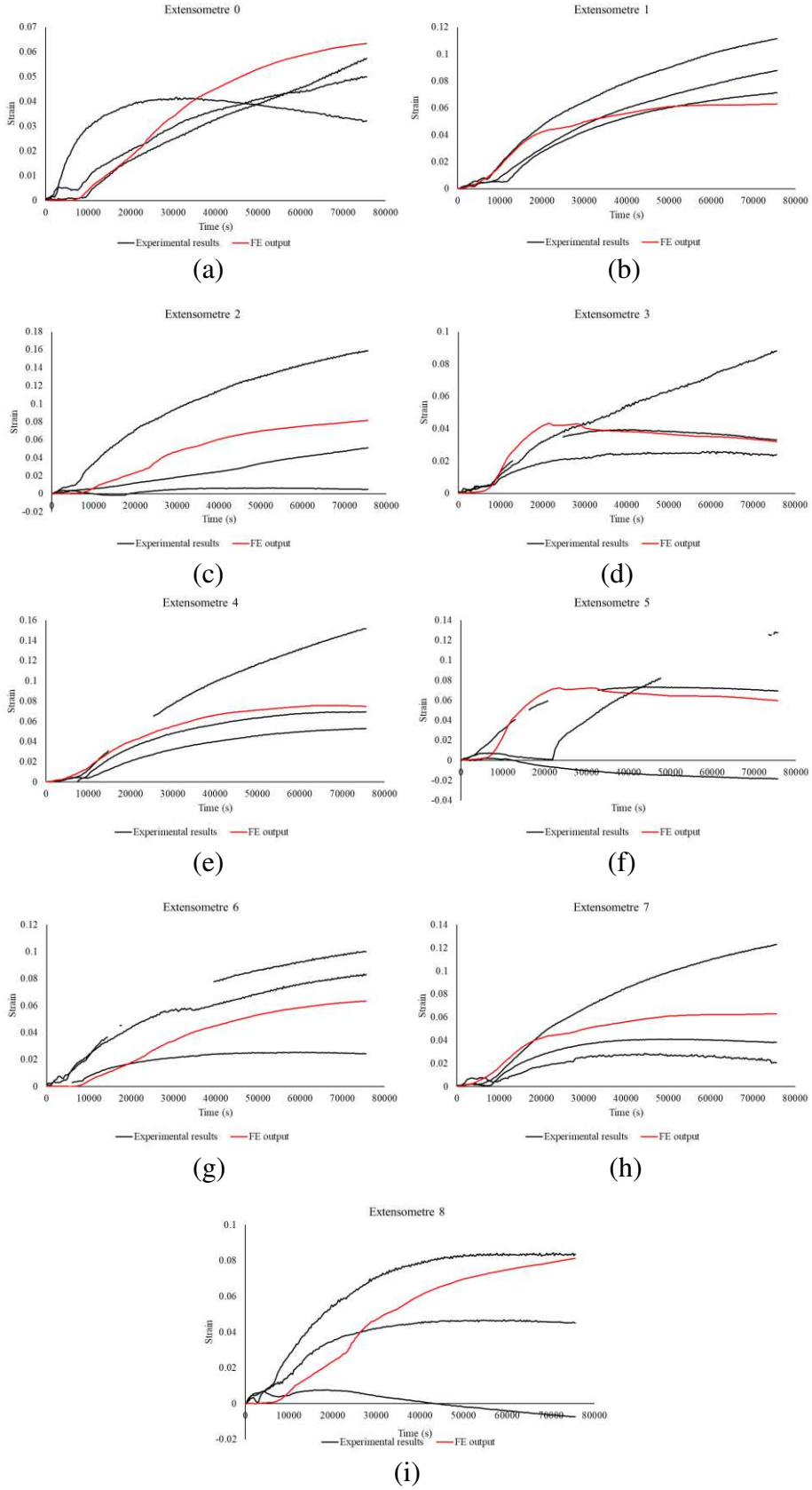

Figure 13. Experimental and numerical comparison of the measurements of the virtual extensometers for the 3D SPG glulam samples (a) E0 to (i) E8

7. Discussion on the delamination process of SPG glulam

Figure 14 shows the variation in moisture content of the 3D glulam specimens extracted from the model at six different drying times. At 3600 s in Figure 14 (b) (i.e., about half the time before delamination develops), the moisture content at the surface of the specimens and up to a depth of 2 mm, has dropped from more than 16 % at the beginning of the drying process to less than 12%. At the onset of delamination (6300 s and Figure 14 (c)), the sides are drier (below 8%) than the end-grain surfaces (RT planes at about 11%). As the drying progresses, all surfaces have dried to less than 8% at 12600 s (Figure 14 (d)). From then (Figure 14 (e)) the moisture at the surface dries to less than 6% and the depth at which the moisture content is less than 6% increases until the end of the 21 h of drying (Figure 14 (f)). In the first few hours of drying, Figure 14 (a) to (d) show steep moisture gradients within the specimens which is becoming more gradual (Figure 14 (e) and (f)) as the drying progresses. This correlates with the rate of glueline delamination in Figure *13* which typically decreases with increasing drying time. Therefore, solutions to limit the sharpness of the moisture gradient during the drying process may reduce delamination.

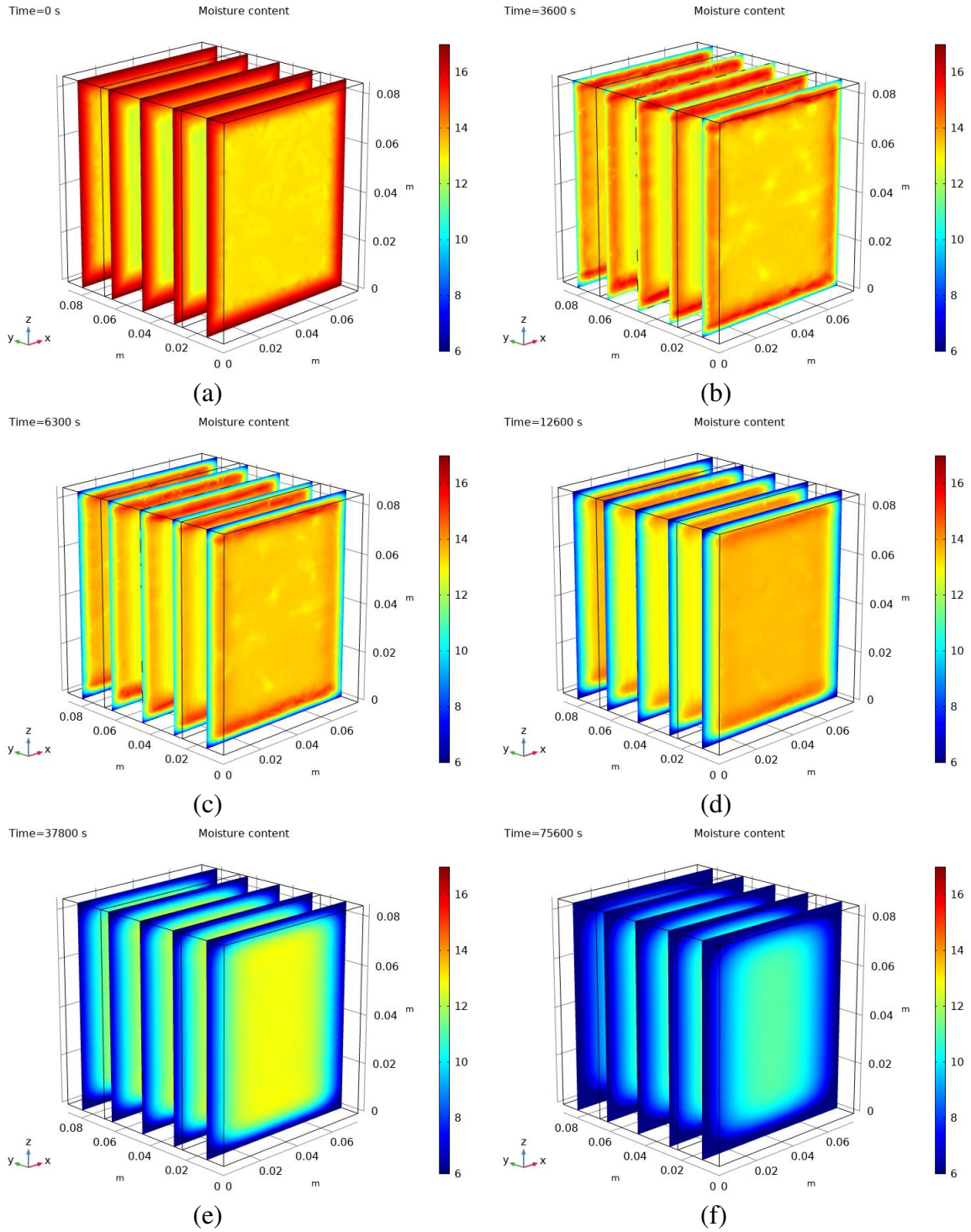

Figure 14. The moisture content of the SPG glulam at (a) 0 s, (b) 3600 s, (c) 6300 s (onset of delamination), (d) 12600 s, (e) 37800 s and (f) 75600 s (end of drying)

To investigate the delamination process, Figure 15 plots the damage factor in the gluelines obtained from Equation (56) at the same time steps as Figure 14. The model shows that delamination developed on the end-grain surfaces (i.e., surfaces parallel to the yz plane in Figure 15) and in the middle of the gluelines (Figure 15 (a)) to rapidly propagates to the corners of the specimens as the gluelines open (Figure 15 (b)). The cracks then propagate deeper into

the specimens and to the side surfaces (Figure 15 (c)). Halfway through the drying process (Figure 15 (d)), the cracks have propagated to all surfaces and are extended deeper into the specimens until the end of the drying process (Figure 15 (e)). Additionally, and as shown in Figure 15 (d) and (e), the delamination is more pronounced for the external gluelines than the internal one. Therefore, solutions to prevent delamination should target the end-grain surfaces and external gluelines as priority.

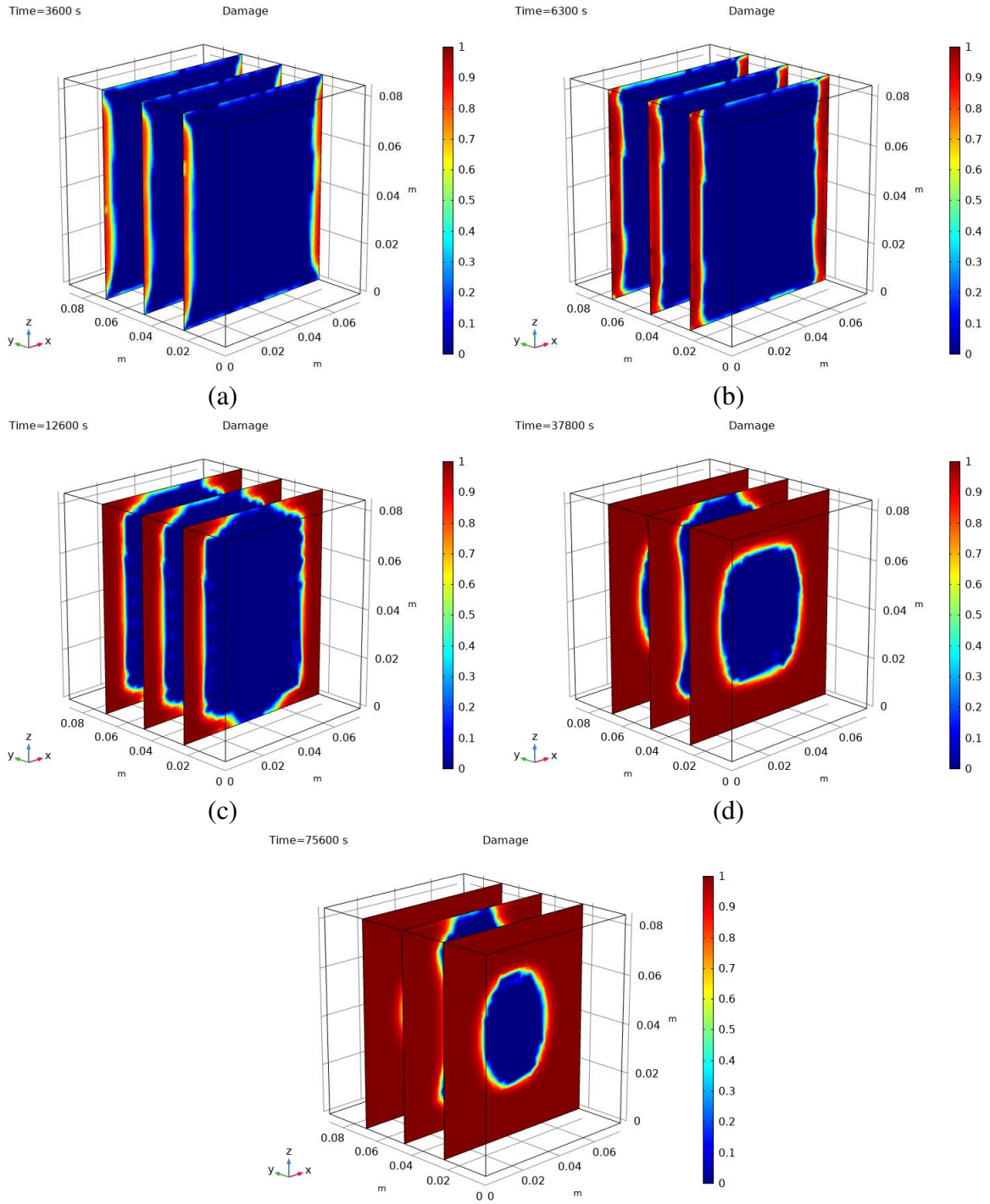

Figure 15. The damage factor of the SPG glulam at (a) 3600 s, (b) 6300 s (onset of delamination), (c) 12600 s, (d) 37800 s and (e) 75600 s (end of drying)

To shed further light on the reasons being the delamination of the SPG glulam, Figure 16 plots the tensile stress to strength and the shear stress to strength ratios in the gluelines at 3600 s, i.e., just before delamination occurs. It can be seen from Figure 16 (a) that the tensile stress to strength ratio is close to 1.0 in the regions where delamination first develops (Figure 15). The shear stress to strength ratios for the two shear planes of the cohesive zone surface is however

less than 0.1, as plotted in Figure 16 (a) and (c). Therefore, delamination principally occurs due to the tensile stress applied to the gluelines during the bond integrity test. Mechanical solutions to prevent delamination must reduce the tensile stress, by changing for instance the profile of the boards to increase the gluing surfaces.

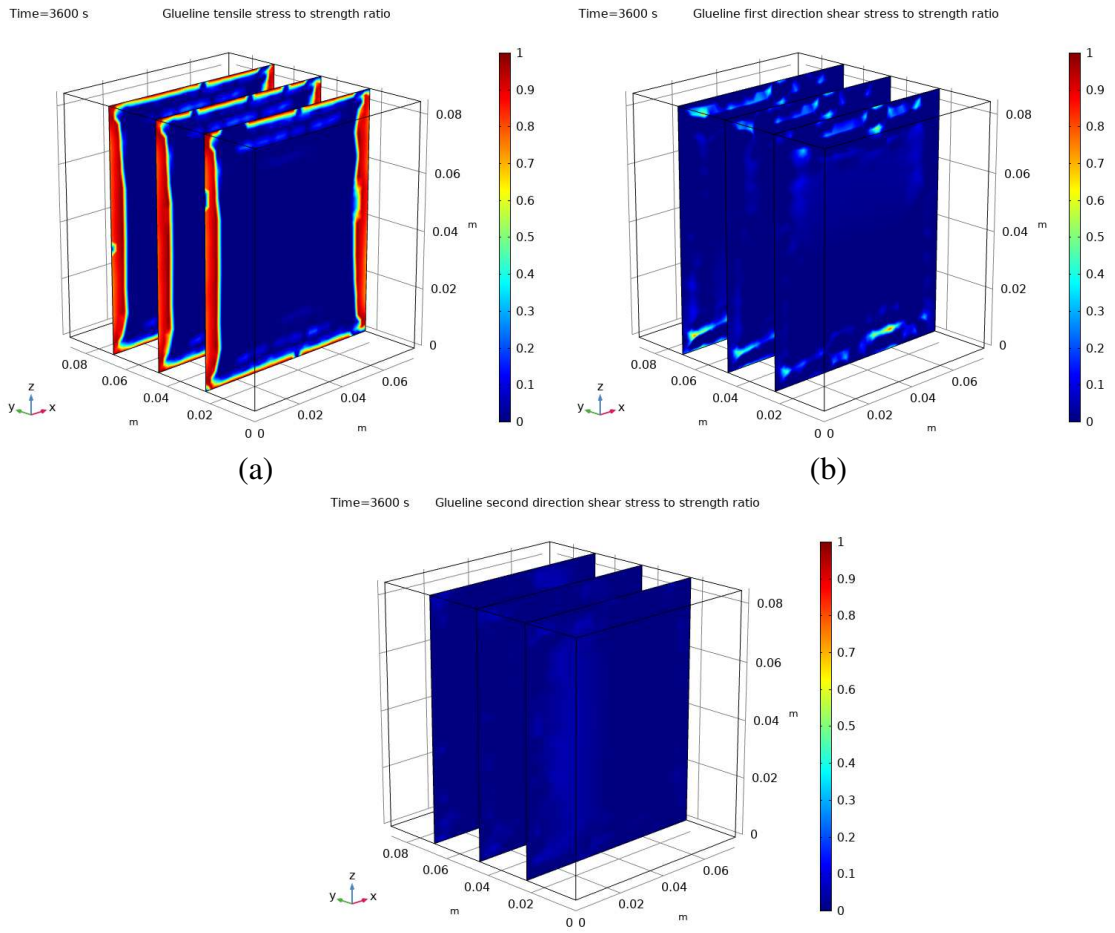

(a) (b)

(c)

Figure 16. Stress to strength ratio at 3600 s (before delamination develops) in the gluelines for (a) tensile (normal to gluelines), (b) shear in first plane and (c) shear in second plane

8. Conclusion

In this study, a 3D numerical model which simulates the bond integrity test in the AS/NZS 1328.1 (1998) by combining a heat and mass transfer model to plasticity and fracture mechanical models was developed and detailed. First, the heat and mass transfer model was validated against 1D experimental tests on single SPG sawn timber boards, with moisture movement in either the longitudinal or perpendicular to grain direction. Model inputs were either determined experimentally or extracted from the literature. Second, the combined heat and mass transfer and mechanical model was validated against experimental tests performed on 3D SPG glulam samples. The model was found to accurately predict (1) the moisture loss

variation of the 3D glulam samples and (2) the delamination process versus time, both in terms of the time at which the gluelines start to delaminate and the rate at which they are opening.

The validated model was finally used to understand the delamination process of SPG glulam to obtain the fundamental knowledge to eventually find solutions to pass the bond integrity test and land the market. It was found that sharp moisture gradients were present within the specimens at the beginning of the drying process. Delamination first developed on the end-grain surfaces to propagate deeper and to the sides of the specimens. Results also indicated that the delamination principally occurred due to the tensile stress applied to the gluelines. Mechanical solutions to prevent delamination would therefore have to reduce the tensile stress applied in the gluelines, especially at the end-grain surfaces.

.

Acknowledgments

The authors would like to thank the technical team at the Salisbury Research Facility of the Queensland Department of Agriculture and Fisheries for helping with the preparation of specimens. This research was supported by the Australian Centre for International Agricultural Research, project FST/2019/128.

Author contributions

Peiqing Lu: Conceptualization, Methodology, Sample manufacturing, Experiment, Simulation, Analysis, Writing, Visualization. Benoit P. Gilbert: Conceptualization, Methodology, Experiment, Simulation, Analysis, Writing, Revision, Visualization, Supervision. Chandan Kumar: Conceptualization, Simulation, Methodology, Sample manufacturing, Revision, Supervision. Robert L. McGavin: Conceptualization, Sample manufacturing, Revision, Supervision. Hassan Karampour: Conceptualization, Revision, Supervision.

Data availability

Data will be available upon request.

Conflict of interest

The authors declare no conflict of interest.

REFERENCES

Aicher, S., & Dill-Langer, G. (1997). Climate induced stresses perpendicular to the grain in glulam. *Otto Graf Journal, 8*, 209-231.
Aicher, S., & Klöck, W. (2001). Linear versus quadratic failure criteria for inplane loaded wood based panels. *Otto-Graf-Journal, 12*, 187.
Angst, V. (2012). *Moisture Induced Stresses in Glulam*. Norwegian University of Science and Technology, PhD thesis,
Angst, V., & Malo, K. A. (2010). Moisture induced stresses perpendicular to the grain in glulam: review and evaluation of the relative importance of models and parameters. *Wood research and technology, 64*(5).
AS/NZS 1080.1. (2012). Timber-Methods of test Method 1: Moisture Content. In. Sydney, Australia: Standards Australia.
AS/NZS 1328.1. (1998). Glued laminated structural timber, Part 1: Performance requirements and minimum production requirements. In. Sydney, Australia: Standards Australia.
Bird, R. B. (2002). Transport phenomena. *Appl. Mech. Rev., 55*(1), R1-R4.
Bootle, K. R. (1983). *Wood in Australia. Types, properties and uses*: McGraw-Hill book company.
Carr, E. J., Turner, I. W., & Perre, P. (2013). A variable-stepsize Jacobian-free exponential integrator for simulating transport in heterogeneous porous media: Application to wood drying. *Journal of Computational Physics, 233*, 66-82.
Çengel, Y. A., & Boles, M. A. (2006). Mass and energy analysis of control volumes. *Thermodynamics: An Engineering Approach*, 216-246.
Cheng, X., Gilbert, B. P., Guan, H., Dias-da-Costa, D., & Karampour, H. (2022). Influence of the earthquake and progressive collapse strain rate on the structural response of timber dowel type connections through finite element modelling. *Journal of Building Engineering, 57*, 104953.
COMSOL Multiphysics. (2019). *COMSOL Multiphysics Reference Manual*. Retrieved from https://doc.comsol.com › com.comsol.help.comsol
Couture, F., Jomaa, W., & Puiggali, J.-R. (1996). Relative permeability relations: a key factor for a drying model. *Transport in Porous Media, 23*, 303-335.
Dahlblom, O., Ormarsson, S., & Petersson, H. (1996). *Simulation of wood deformation processes in drying and other types of environmental loading.* Paper presented at the Annales des sciences forestieres.
Dymond, J. H. (1999). Handbook of Physical Properties of Liquids and Gases Pure Substances and Mixtures. Third Augmented and Revised Edition. By NB Vargaftik, YK Vinogradov, and VS Yargin. Begell House, Inc., New York. 1996. 1359 pp. $165.00. ISBN 1-56700-063-0. In: ACS Publications.
Faircloth, A., Gilbert, B., Chandan, K., William, L., & Robert, M. (2024). Understanding the Adhesion Performance of Glued Laminated Timber Manufactured with Australian Softwood and Hardwood Species. *Wood Science and Technology (in preparation)*.
Franke, B., & Quenneville, P. (2011). Numerical modeling of the failure behavior of dowel connections in wood. *Journal of Engineering Mechanics, 137*(3), 186-195.
Gezici-Koç, Ö., Erich, S. J., Huinink, H. P., Van der Ven, L. G., & Adan, O. C. (2017). Bound and free water distribution in wood during water uptake and drying as measured by 1D magnetic resonance imaging. *Cellulose, 24*, 535-553.
Gilbert, B. P., Dias-da-Costa, D., Lebée, A., & Foret, G. (2020). Veneer-based timber circular hollow section beams: behaviour, modelling and design. *Construction and building materials, 258*, 120380.
Guitard, D., & El Amri, F. (1987). *Modèles prévisionnels de comportement élastique tridimensionnel pour les bois feuillus et les bois résineux.* Paper presented at the Annales des sciences forestières.

Hanhijärvi, A. (1999). Deformation properties of Finnish spruce and pine wood in tangential and radial directions in association to high temperature drying Part II. Experimental results under constant conditions (viscoelastic creep) Part II. Experimental results under constant conditions (viscoelastic creep). *Holz als Roh-und Werkstoff, 57*, 365-372.

Hanhijärvi, A. (2000). Advances in the knowledge of the influence of moisture changes on the long-term mechanical performance of timber structures. *Materials and Structures, 33*, 43-49.

Kumar, C., Joardder, M., Farrell, T. W., & Karim, M. (2016). Multiphase porous media model for intermittent microwave convective drying (IMCD) of food. *International Journal of Thermal Sciences, 104*, 304-314.

Kumar, C., Joardder, M. U. H., Farrell, T., Millar, G., & Karim, A. (2014). *Multiphase porous media model for heat and mass transfer during drying of agricultural products.* Paper presented at the Proceedings of the 19th Australasian Fluid Mechanics Conference.

Leggate, W., McGavin, R. L., Miao, C., Outhwaite, A., Chandra, K., Dorries, J., . . . Knackstedt, M. (2020). The influence of mechanical surface preparation methods on southern pine and spotted gum wood properties: Wettability and permeability. *BioResources, 15*(4), 8554.

Leggate, W., McGavin, R. L., Outhwaite, A., Dorries, J., Robinson, R., Kumar, C., . . . Knackstedt, M. (2021a). The Influence of Mechanical Surface Preparation Method, Adhesive Type, and Curing Temperature on the Bonding of Darwin Stringybark. *BioResources, 16*(1).

Leggate, W., McGavin, R. L., Outhwaite, A., Gilbert, B. P., & Gunalan, S. (2022a). Barriers to the Effective Adhesion of High-Density Hardwood Timbers for Glue-Laminated Beams in Australia. *Forests, 13*(7). doi:https://doi.org/10.3390/f13071038

Leggate, W., Outhwaite, A., McGavin, R. L., Gilbert, B. P., & Gunalan, S. (2022b). The Effects of the Addition of Surfactants and the Machining Method on the Adhesive Bond Quality of Spotted Gum Glue-laminated Beams. *BioResources, 17*(2), 3413-3434.

Leggate, W., Shirmohammadi, M., McGavin, R. L., Outhwaite, A., Knackstedt, M., & Brookhouse, M. (2021b). Examination of Wood Adhesive Bonds via MicroCT: The Influence of Pre-Gluing Surface Machining Treatments for Southern Pine, Spotted Gum, and Darwin Stringybark Timbers. *BioResources, 16*(3).

Lu, P., Gilbert, B. P., Kumar, C., McGavin, R. L., & Karampour, H. (2023). Influence of the moisture content on the fracture energy and tensile strength of hardwood spotted gum sawn timber and adhesive bonds (gluelines). *European Journal of Wood and Wood Products*, 1-16.

MacLean, J. (1941). Thermal conductivity of wood. *Heating, piping & air conditioning. Madison, USA*.

Mårtensson, A. (1994). Creep behavior of structural timber under varying humidity conditions. *Journal of Structural Engineering, 120*(9), 2565-2582.

Ni, H., Datta, A., & Torrance, K. (1999). Moisture transport in intensive microwave heating of biomaterials: a multiphase porous media model. *International Journal of Heat and Mass Transfer, 42*(8), 1501-1512.

Ormarsson, S. (1999). *Numerical analysis of moisture-related distortion in sawn timber.* Chalmers University of Technology, Dep. of Structural Mech,

Ormarsson, S., Dahlblom, O., & Petersson, H. (1998). A numerical study of the shape stability of sawn timber subjected to moisture variation Part 1: Theory. *Wood Science and Technology, 32*, 325-334.

Pang, S. (2001). *Modelling of stresses and deformation of radiata pine lumber during drying.* Paper presented at the Proc. 7th International IUFRO Wood Drying Conference, Tsukuba, Japan.

Perré, P. (1996). *The numerical modelling of physical and mechanical phenomena involved in wood drying: an excellent tool for assisting with the study of new processes.* Paper presented at the Proc. 5th International IUFRO Wood Drying Conference, Québec, Canada.

Perré, P. (2007). *Fundamentals of wood drying*: AR BO. LOR Nancy.

Perré, P., & Turner, I. (2001). Determination of the material property variations across the growth ring of softwood for use in a heterogeneous drying model. Part 2. Use of homogenisation to predict bound liquid diffusivity and thermal conductivity.

Perré, P., & Turner, I. W. (1999). Transpore: a generic heat and mass transfer computational model for understanding and visualising the drying of porous media. *Drying Technology, 17*(7-8), 1273-1289.

Perré, P., & Turner, I. W. (2008). A mesoscopic drying model applied to the growth rings of softwood: mesh generation and simulation results. *Maderas. Ciencia y tecnología, 10*(3), 251-274.

Perussello, C. A., Kumar, C., de Castilhos, F., & Karim, M. (2014). Heat and mass transfer modeling of the osmo-convective drying of yacon roots (Smallanthus sonchifolius). *Applied Thermal Engineering, 63*(1), 23-32.

Queensland Government Department of Agriculture and Fisheries. (2016). *Queensland Forest & Timber Industry. An Overview*.

Raftery, G. M., & Whelan, C. (2014). Low-grade glued laminated timber beams reinforced using improved arrangements of bonded-in GFRP rods. *Construction and building materials, 52*, 209-220.

Ranta-Maunus, A. (1993). Rheological behaviour of wood in directions perpendicular to the grain. *Materials and Structures, 26*, 362-369.

Redman, A. (2017). *Modelling of vacuum drying of Australian hardwood species.* (PhD thesis PhD thesis). Queensland University of Technology, PhD thesis,

Redman, A., Bailleres, H., Gilbert, B. P., Carr, E. J., Turner, I. W., & Perré, P. (2018). Finite element analysis of stress-related degrade during drying of Corymbia citriodora and Eucalyptus obliqua. *Wood Science and Technology, 52*, 67-89.

Redman, A., Bailleres, H., & Perré, P. (2011). Characterization of viscoelastic, shrinkage and transverse anatomy properties of four Australian hardwood species. *Wood Material Science & Engineering, 6*(3), 95-104.

Redman, A., Bailleres, H., Turner, I., & Perré, P. (2012). Mass transfer properties (permeability and mass diffusivity) of four Australian hardwood species. *BioResources, 7*(3), 3410-3424.

Redman, A., Bailleres, H., Turner, I., & Perré, P. (2016). Characterisation of wood–water relationships and transverse anatomy and their relationship to drying degrade. *Wood Science and Technology, 50*, 739-757.

Ross, R. J. (2010). Wood handbook: wood as an engineering material. *USDA Forest Service, Forest Products Laboratory, General Technical Report FPL-GTR-190, 2010: 509 p. 1 v., 190*.

Salin, J.-G. (1992). Numerical prediction of checking during timber drying and a new mechano-sorptive creep model. *Holz als Roh-und Werkstoff, 50*(5), 195-200.

sandoval Torres, S., Jomaa, W., Puiggali, J.-R., & Avramidis, S. (2011). Multiphysics modeling of vacuum drying of wood. *Applied Mathematical Modelling, 35*(10), 5006-5016.

Seredyński, M., Wasik, M., Łapka, P., Furmański, P., Cieślikiewicz, Ł., Pietrak, K., . . . Jaworski, M. (2020). Analysis of non-equilibrium and equilibrium models of heat and moisture transfer in a wet porous building material. *Energies, 13*(1), 214.

Skaar, C. (2012). *Wood-water relations*: Springer Science & Business Media.

Toratti, T., & Svensson, S. (2000). Mechano-sorptive experiments perpendicular to grain under

tensile and compressive loads. *Wood Science and Technology, 34*(4), 317-326.
Turner, I. W. (1996). A two-dimensional orthotropic model for simulating wood drying processes. *Applied Mathematical Modelling, 20*(1), 60-81.
Turner, I. W., & Perré, P. (2004). Vacuum drying of wood with radiative heating: II. Comparison between theory and experiment. *AIChE Journal, 50*(1), 108-118.
Vega-Mercado, H., Góngora-Nieto, M. M., & Barbosa-Cánovas, G. V. (2001). Advances in dehydration of foods. *Journal of Food Engineering, 49*(4), 271-289.
Whitaker, S. (1977). Simultaneous heat, mass, and momentum transfer in porous media: a theory of drying. In *Advances in heat transfer* (Vol. 13, pp. 119-203): Elsevier.